Mutual synchronization of self-excited acoustic oscillations in coupled thermoacoustic oscillators

Geng Chen[1, *], Zhaoyu Li[2], Lihua Tang[2], Zhibin Yu[3]

1. National Engineering Research Center of Turbo-Generator Vibration, School of Energy and Environment, Southeast University, Nanjing 210096, China
2. Department of Mechanical Engineering, University of Auckland, Auckland, 1010, New Zealand
3. James Watt School of Engineering, University of Glasgow, Glasgow G12 8QQ, UK

ABSTRACT

Synchronization refers to the adjustment of rhythms of two nonidentical oscillators due to interaction. In this study, we report for the first time on the ability of computational fluid dynamics (CFD) to simulate the synchronization of self-sustained acoustic oscillations in two coupled thermoacoustic oscillators that interfere with each other through acoustic radiation. A bifurcation diagram containing both asynchronous and synchronous states is first mapped out by changing the end-to-end distance and the resonator length difference. It is found that the two thermoacoustic oscillators are analogous to mutually coupled Van der Pol oscillators with reactive coupling. Then, the dynamic characteristics of beating and periodic oscillations in asynchronous and synchronous states are analysed separately to facilitate the comprehension of the synchronization process. This research demonstrates that the CFD methodology provides a valuable numerical tool for studying the synchronization of thermally-induced acoustic oscillations in thermoacoustic systems.

Keywords: Synchronization; Thermoacoustic engine; Computational fluid dynamics; Bifurcation diagram; Beating;

1. Introduction

Thermoacoustic engines (TAEs) are essentially the acoustic equivalents of traditional gas-cycle engines [1]. They rely on the thermoacoustic effect to convert low-grade heat such as industrial waste heat, solar energy, geothermal energy, etc, into high-amplitude acoustic oscillations using no/few moving components and environmentally friendly working fluids [2]. The study of thermoacoustic effect is multi-disciplinary since it involves fundamentals of heat transfer, thermodynamics, fluidic mechanics, acoustics, and nonlinear dynamics, to name a few [3]. This allows researchers from various backgrounds to participate in the thermoacoustic research and study thermoacoustics from different aspects [4-6].

[*] Correspondent author: chengeng@seu.edu.cn

Most of the previous research on TAEs focused on the reduction of onset temperature or improvement of thermoacoustic power generation for practical use [7-9]. The linear thermoacoustic theory developed by Rott [10] and Swift [11] is often used in those studies to predict the stability limit and optimize the energy conversion. However, nonlinearity arises as the acoustic pressure amplitude becomes high (e.g., greater than 10% of the mean pressure [12]). In this situation, the linear theory is less accurate, and nonlinear theoretical or numerical methodologies should be adopted [13]. Common nonlinear effects encountered in TAEs include shock waves [14], minor losses [15], mass streaming [16], onset of turbulence [17], onset of chaos [18-20], etc. Recently, there is a growing interest in studying the nonlinear dynamic behaviour of thermoacoustic devices. For example, Chen [21] investigated the bi-stable nature of a standing-wave TAE and triggering of thermoacoustic instability via an external disturbance. Biwa [22] and Hyodo [23] attempted to introduce oscillation death in coupled TAEs by using a needle valve and/or hollow tubes.

Synchronization is another nonlinear dynamic behaviour reported in TAEs. It refers to the process in which the TAE oscillates not at its own natural frequency, but at the frequency of a periodic external force or another TAE. Synchronization of a TAE by an external force has been reported by Penelet [24] and Sato [25]. In Ref. [24], the TAE exhibited periodic oscillations and was synchronized by a loudspeaker. Synchronization regions called *Arnold tongues* were measured as functions of the loudspeaker voltage and frequency. In Ref. [25], synchronization of quasiperiodic oscillations by a piston was investigated. Bifurcation diagrams were mapped out by changing the forcing strength and frequency. Mutual synchronization of TAEs has been explored by Spoor and Swift [26, 27] who adopted a duct to connect the two TAEs and enforced mode locking for vibration cancellation. Inspired by their research, Delage [28] investigated the coupling of two chaotic TAEs by a plate with an orifice. It is found that the coupled chaotic TAEs experienced on-off intermittency when the complete synchronization broke down by decreasing the orifice size.

Despite being reported in a few studies, synchronization of acoustic oscillations in TAEs received little attention. One major reason is that most researchers studied thermoacoustics from the aspects of thermodynamics and heat transfer. From a nonlinear dynamic perspective, synchronization offers a viable approach to control the behaviour of self-oscillating systems by means of inexpensive perturbations [29]. However, research on the synchronization of self-sustained thermoacoustic oscillations is still lacking. In this study, we numerically investigated the mutual synchronization of thermally-induced acoustic oscillations in coupled TAEs. Computational fluid dynamics (CFD) is employed to study the synchronization process. To the best of our knowledge, there has been no CFD modelling of synchronization in TAEs in the literature. The CFD method in this study provides a powerful tool to investigate synchronization of acoustic oscillations initiated by heat. The rest of this paper is organized as follows. Section 2 introduces the coupled TAEs under investigation. Section 3

describes the CFD methodology. Section 4 discusses the synchronization phenomenon. Finally, the concluding remarks are presented in Section 5.

2. Model description

Figure 1 displays the coupled thermoacoustic oscillators under investigation. Two quarter-wavelength standing-wave thermoacoustic engines (TAEs) are placed coaxially with their open ends facing each other. Each TAE is composed of a hot buffer, a parallel-plate stack sandwiched between a pair of hot (red lines) and ambient (blue lines) heat exchangers, and an acoustic resonator. The heat exchangers create a temperature gradient across the stack. As the temperature gradient reaches a critical (or onset) value, the working fluid inside the TAE oscillates spontaneously due to the thermoacoustic effect. In this sense, a TAE can be called a thermoacoustic (TA) oscillator. In Fig. 1, the two TA oscillators (TA oscillator 1 and TA oscillator 2) are interfering with each other via acoustic radiation in the space between the open ends.

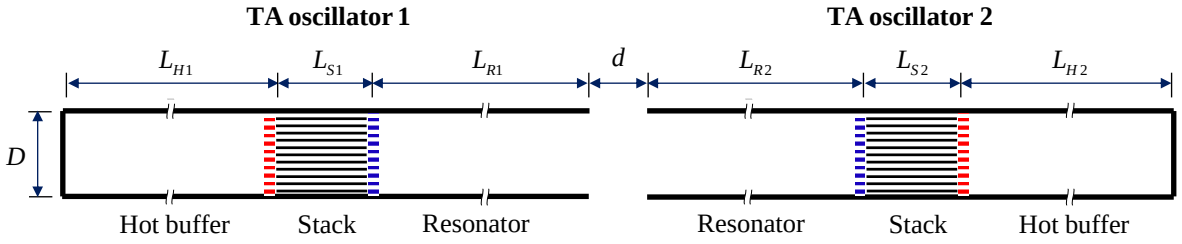

Figure 1. Schematic of the coupled thermoacoustic oscillators. The red and blue lines at the stack ends represent the hot and cold heat exchangers.

In this study, atmospheric air is chosen as the working fluid. The hot buffer and hot heat exchanger have a surface temperature of T_h = 900 K, while the ambient heat exchanger and resonator have a surface temperature of T_c = 300 K. The surface temperature decreases linearly from T_h to T_c in the stack. Table 1 lists the key geometrical parameters of the baseline thermoacoustic oscillator. In the following research, the end-to-end distance d and the resonator length L_{R2} of oscillator 2 will be adjusted, and their influence on the dynamic behaviour of the coupled thermoacoustic oscillators will be investigated.

Table 1. Key geometrical parameters of the baseline thermoacoustic oscillator.

Parameters	**Values**
Diameter D	0.013 m
Hot buffer length L_H	0.1 m
Stack length L_S	0.03 m
Resonator length L_R	0.12 m
Stack plate thickness t_S	1×10^{-3} m
Gap between stack plates d_S	1×10^{-3} m

3. CFD modelling

Computational fluid dynamics (CFD) simulations are conducted to study the spontaneous acoustic oscillations in the coupled thermoacoustic oscillators.

3.1 Model configuration

Figure 2 shows mesh configuration of the 2-D (two-dimensional) computational model established for the proposed coupled thermoacoustic oscillators. High-resolution structured quad grids are adopted in the meshing process. In the figure, the grids belonging to the TAEs and outfield (whose size is 0.05 m×0.05 m) are marked in black and blue, respectively. To save computational cost, the pair of heat exchangers and the solid stack plates are omitted. Instead, only 6 fluid channels between the stack plates are meshed for each TAE. The grids inside one fluid channel and in the vicinity of the open ends are shown in the enlarged views. Note that, to capture the thermoacoustic effect accurately, the maximum grid size in transverse direction in the stack channels should be no larger than 1×10^{-4} m, which is the order of the magnitude of thermal penetration depth at ambient temperature and natural frequency.

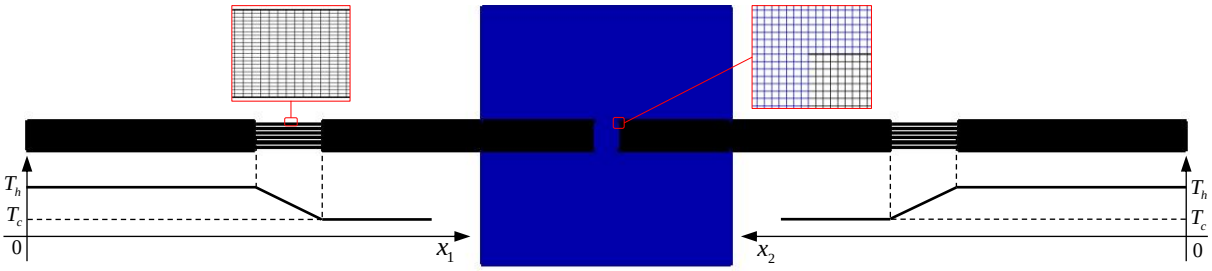

Figure 2. Mesh configuration of the coupled thermoacoustic oscillators. The black grids belong to fluid domain of the thermoacoustic oscillators. The blue grids belong to the outfield.

In the CFD modelling, non-slip boundary conditions are imposed on the wall surfaces. As shown in Fig. 2, isothermal boundary conditions are applied on the wall surfaces of the hot buffer and resonator. A user-defined function (UDF) is adopted to realize the linear temperature distribution along the stack. A pressure outlet (p = 0) is imposed on the edges of the outfield. The working fluid (i.e., air) is assumed to be a compressible ideal gas. It follows the Navier-Stokes equations and the equation of state, which are [30]

$$\frac{\partial \bar{\rho}}{\partial t}+\frac{\partial}{\partial x_i}\left(\bar{\rho}\tilde{u}_i\right)=0 \tag{1}$$

$$\frac{\partial}{\partial t}\left(\bar{\rho}\tilde{u}_i\right)+\frac{\partial}{\partial x_j}\left(\bar{\rho}\tilde{u}_i\tilde{u}_j+\bar{p}\delta_{ij}-\bar{\tau}_{ij}^{tot}\right)=0 \tag{2}$$

$$\frac{\partial}{\partial t}\left(\bar{\rho}\tilde{e}_{tot}\right)+\frac{\partial}{\partial x_j}\left(\bar{\rho}\tilde{u}_j\tilde{e}_{tot}+\tilde{u}_j\bar{p}+\bar{q}_j^{tot}-\tilde{u}_i\bar{\tau}_{ij}^{tot}\right)=0 \tag{3}$$

$$p = \rho R_g T \tag{4}$$

where the overbars "~" and "–" denote the density-weighted time averaging (Favre averaging) and classical time averaging (Reynolds averaging), respectively. p, ρ and T are pressure, density and temperature, u_i or u_j stands for the velocity component in corresponding direction, $e_{tot} = e + u_i u_i / 2$ is the total energy with e being the specific internal energy, τ_{ij}^{tot} is the total stress tensor, q_j^{tot} is the heat flux, δ_{ij} is the Kronecker delta, and R_g is the specific gas constant.

Equations (1) to (4) are resolved numerically using the commercial CFD package FLUENT 18.1 [31] that adopts a pressure-based finite volume method. In the simulations, the PISO (Pressure-Implicit Splitting Operators) scheme is used for pressure-velocity coupling, the second order upwind approach is employed for spatial discretization, and the second-order implicit algorithm is adopted for temporal discretization. The standard k-ε turbulence model, that contains two transport equations for the turbulence kinetic energy k and rate of dissipation ε, is adopted to account for the turbulence effects [32]. Note that the standard k-ε model has been successfully implemented to simulate thermoacoustic oscillations in previous studies [33-35].

In this study, we follow two steps to obtain spontaneous thermoacoustic oscillations via CFD. First, pressure inlets (gauge pressure 1 Pa) at $x_1 = 0$ and $x_2 = 0$ are enabled, and a steady calculation is performed. Once convergence is achieved, the pressure inlets are replaced by rigid walls. Then, a transient calculation is conducted, and the acoustic pressure p_1 at $x_1 = 0$ and p_2 at $x_2 = 0$ are monitored.

3.2 Sensitivity study

Sensitivity studies are conducted to investigate the dependence of CFD results on the grid and timestep sizes. In the grid size independence study, the grid size in the stack region varies while it is fixed at 0.5 mm for the rest of the fluid domain. It is found that the amplitude of p_1 in the transient calculation decreases and asymptotes as the maximum grid size decreases. The optimal grid size in the stack region is chosen at 0.02 mm as further decreasing the grid size causes negligible (less than 0.1%) changes of the pressure amplitude but increases the computational cost significantly. The optimal grid size is adopted in the meshing of coupled thermoacoustic oscillators with different d and L_{R2}. In the timestep size independence study, the timestep size is decreased from a large value to a small value. Results show that the pressure amplitude increases and levels off as the timestep size decreases. It is found that 10 μs is small enough to accurately capture thermoacoustic effect while minimizing the computational cost simultaneously. Therefore, the optimal timestep size is chosen at 10 μs, and is used in the transient calculations of acoustic pressure oscillations in the coupled thermoacoustic oscillators meshed above.

4. Results and discussion

In this section, we investigate the dynamic characteristics of coupled thermoacoustic oscillators by means of bifurcation diagram, Fast Fourier Transform, wavelet transform, phase space plots, etc.

4.1 Single TA oscillator

Prior to the investigation of coupled TA oscillators, the dynamic behaviour of a single TA oscillator is explored. When simulating a single TA oscillator, we remove the TA oscillator 2 in Fig. 2 but keep the outfield; T_h and T_c are maintained at 900 K and 300 K, respectively. Figure 3(a) displays the time history of acoustic pressure at x_1 = 0 for the baseline TA oscillator (L_R = 120 mm). The acoustic pressure undergoes exponential growth and nonlinear saturation before reaching the steady state where periodic oscillations occur. The frequency f and amplitude p_A of the steady-state limit-cycle oscillations can be decided by the time difference between two adjacent peaks and the peak value. At L_R = 120 mm, f = 375.9 Hz and p_A = 5,104 Pa. Figure 3(b) shows the dependence of p_A and f on L_R. As L_R changes from 90 mm to 150 mm, f decreases from 425.5 Hz to 335.6 Hz. This is because the acoustic wavelength increases as L_R increases, thus reducing the natural frequency of thermoacoustic system. Meanwhile, p_A decreases from 6,002 Pa to 3,581 Pa as L_R increases. Two reasons may account for this feature. First, the stack is relatively closer to the velocity node (rigid end) as L_R increases, resulting in smaller acoustic power generation. Secondly, the increase of L_R causes larger viscous losses in the acoustic resonator.

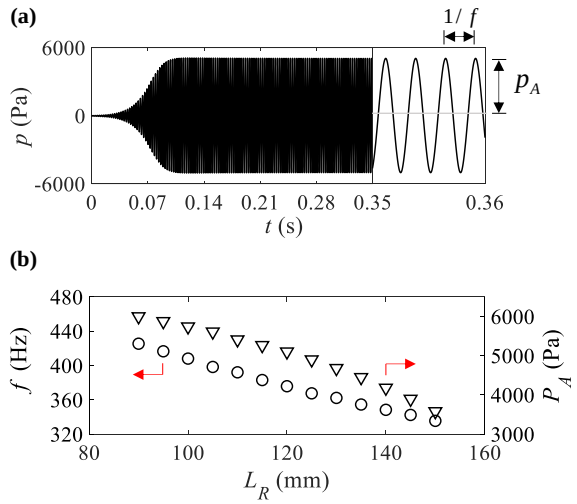

Figure 3. Performance of single TA oscillators. (a) Time series of closed-end pressure oscillations of the baseline TA oscillator. (b) Dependence of limit-cycle frequency f and amplitude p_A on L_R. T_h = 900 K and T_c = 300 K.

4.2 Coupled TA oscillators

4.2.1 Bifurcation diagram

The dynamic behaviour of a single TA oscillator changes when coupling with another oscillator. Figure 4 first gives examples of two different states (asynchronous and synchronous) observed in the CFD

simulations. Figure 4(a) depicts the time series of closed-end acoustic pressure (p_1 of oscillator 1) at d = 9 mm, L_{R1} = 120 mm, L_{R2} = 105 mm (also point B in Fig. 5). In this case, the state is asynchronous, and the steady-state response is beating. Figures 4(b) and 4(c) display the corresponding continuous wavelet transforms [36] and the steady-state phase-space trajectories, in which the time delay ζ is chosen as 10^{-3} s [37-39]. Intermittency is clearly visible in the time-frequency image in Fig. 4(b) as a result of the beating effect. Accordingly, the phase-space trajectory exhibits a round pie in Fig. 4(c). Figure 4(d) depicts the time series of closed-end acoustic pressure (p_1 of oscillator 1) at d = 9 mm, L_{R1} = 120 mm, L_{R2} = 110 mm (also point C in Fig. 5). In this case, the state is synchronous, and the steady-state response is periodic oscillations that have a single frequency that is invariant with time (Fig. 4(e)). Accordingly, the phase-space trajectory becomes a single loop as seen in Fig. 4(f). Further examination of p_2 of oscillator 2 (not shown) reveals that both p_1 and p_2 oscillate at 390.6 Hz which is close to the natural frequency (389.1 Hz) of a single oscillator at L_R = 110 mm.

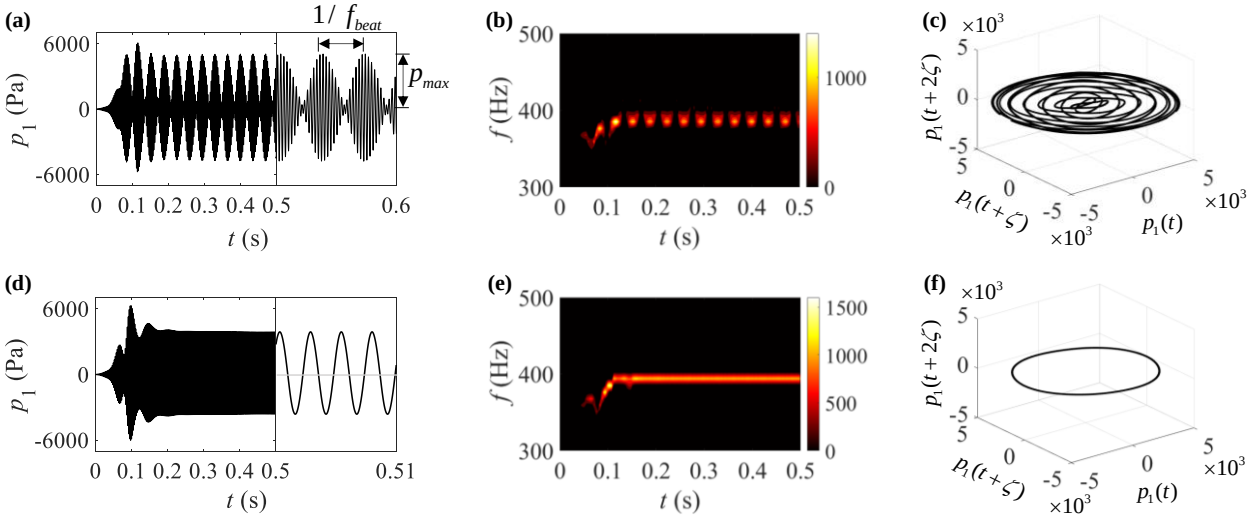

Figure 4. Dynamic characteristics of asynchronous and synchronous states. (a)-(c): asynchronous state; d = 9 mm, L_{R1} = 120 mm and L_{R2} = 105 mm. (d)-(f): synchronous state; d = 9 mm, L_{R1} = 120 mm and L_{R2} = 110 mm. (a) and (d): time histories. (b) and (e): corresponding wavelet transforms. (c) and (f): corresponding steady-state phase space portraits. T_h = 900 K and T_c = 300 K.

Figure 5 depicts the two-parameter bifurcation diagram of steady-state responses of the coupled TA oscillators. To map out the bifurcation diagram, d changes from 5 mm to 15 mm with an increment of 1 mm; L_{R1} is fixed at 120 mm while L_{R2} changes from 90 mm to 120 mm with an increment of 5 mm. As a result,

$$\Delta L_R = L_{R2} - L_{R1} \quad (5)$$

varies from -30 mm to 30 mm. The computational cost of making Fig. 5 is high: it takes around 8×10^6 CPUhs (1 CPUh = 1 CPU×1 hour) to finish all (11×13 = 143) computational tasks. In Fig. 5, region I (composed of ×) represents asynchronous states while region II (composed of •) denotes synchronous

states. The boundaries (solid lines) distinguishing them correspond to the *saddle-node bifurcation* [40]. We can see from the figure that, the smaller d is, the larger $|\Delta L_R|$ can be used to achieve synchronous states.

It is worth mentioning that the bifurcation diagram in Fig. 5 resembles the 1:1 synchronization tongue (Fig. 4.5 in Ref. [29]) for the mutually coupled Van der Pol oscillators. Like many other complex systems, the dynamic behaviour of coupled TA oscillators can be qualitatively described by [29]

$$\begin{cases} \ddot{X}_1 - \left(\lambda_1 - X_1^2\right)\dot{X}_1 + \omega_1^2 X_1 + B_R\left(X_1 - X_2\right) + B_D\left(\dot{X}_1 - \dot{X}_2\right) = 0 \\ \ddot{X}_2 - \left(\lambda_2 - X_2^2\right)\dot{X}_2 + \omega_2^2 X_2 + B_R\left(X_2 - X_1\right) + B_D\left(\dot{X}_2 - \dot{X}_1\right) = 0 \end{cases} \quad (6)$$

where X_1 and X_2 stand for the displacements of the oscillators, λ_1 and λ_2 are non-linearity parameters, ω_1 and ω_2 are eigenfrequencies, and B_R and B_D represent the strength of *reactive* and *dissipative* couplings, respectively. In this study, the coupling between TA oscillators is more reactive than dissipative, i.e., B_R ? B_D, mainly due to the following three reasons. First, the two TA oscillators interfere with each other via acoustic radiation, whose impedance contains an inductive acoustic reactance and an acoustic resistance [41]. The velocity antinode at the open ends intensifies the reactance component. Secondly, a distinctive feature of dissipative coupling is the existence of amplitude death (Fig. 4.1 in Ref. [29]), which is not observed in Fig. 5. Finally, for the dissipative coupling, the oscillation frequency at synchronous states is settled in a value in between the natural frequencies of two subsystems (Fig. 4.2 in Ref. [29]). However, when the coupling is reactive, the two oscillators compete, pull each other and the final frequency at which both subsystems settle at synchronous states is larger than their natural frequencies (Fig. 4.7 in Ref. [29]). In this study, the situation of reactive coupling is substantiated by the numerical results in Fig. 9(b), which will be discussed later in Section 4.2.3.

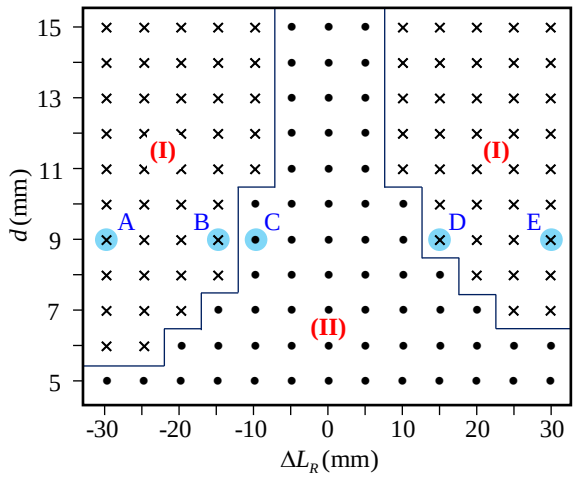

Figure 5. Two-parameter bifurcation diagram. Region I: asynchronous states. Region II: synchronous states. Points A to E are highlighted in shaded circles. T_h = 900 K and T_c = 300 K.

4.2.2 Asynchronous states

To interpret the synchronous states in region II properly, the dynamic characteristics of asynchronous states in region I are first analysed.

Take the asynchronous state at point B in Fig. 5 as an example. As shown in Fig. 6(a), since the two oscillators are not synchronized, the beating effect persists after t = 0.2 s for both p_1 and p_2. There are amplitude modulations of p_1 and p_2 with their maximum values denoted by $p_{1A,\max}$ and $p_{2A,\max}$, respectively. Also denoted in the figure is the time difference $1/f_{beat}$ between two adjacent amplitude maxima with f_{beat} representing the beating frequency. Figure 6(b) presents the FFT (Fast Fourier Transform) of the time-domain signals. For both p_1 and p_2, two slightly different frequencies f_{osc1} and f_{osc2} are observed. The values of f_{osc1} and f_{osc2} are close to the natural frequencies of single oscillators in Fig. 3. According to linear acoustics, the superposition of two sine waves with close frequencies contributes to beats, the frequency of which is the difference between the wave frequencies. This conclusion is verified in this study due to the fact that f_{beat} in Fig. 6(a) equals $|f_{osc1} - f_{osc2}|$ in Fig. 6(b). Figure 6(b) also indicates that the acoustic energy levels of f_{osc1} and f_{osc2} are comparable in p_1 whereas f_{osc2} dominates in p_2. This explains why the envelopes of beating waveforms in Fig. 6(a) are significantly different.

Figure 7 further displays the contours of $p_{1A,\max}$, $p_{2A,\max}$ and their difference $\Delta p_{A,\max} = p_{2A,\max} - p_{1A,\max}$ in region I. In the figure, the arrows point to the descending direction. We can see from the figure that when $\Delta L_R \in$ [-30, -10], $p_{1A,\max}$ increases with increasing d while $p_{2A,\max}$ decreases with decreasing ΔL_R. As a result, $\Delta p_{A,\max}$ decreases along the upper-left direction. Similarly, when $\Delta L_R \in$ [10, 30], $p_{1A,\max}$ increases with decreasing ΔL_R while $p_{2A,\max}$ decreases with decreasing d. As a result, $\Delta p_{A,\max}$ decreases along the down-left direction. It can be also seen in Fig. 7(c) that, $\Delta p_{A,\max} > 0$ when $\Delta L_R \in$ [-30, -10], but $\Delta p_{A,\max} < 0$ when $\Delta L_R \in$ [10, 30]. We further examine the time series (not shown) of p_1 and p_2 at point D in Fig. 5. It is found that the waveforms of p_1 and p_2 at point D are similar to those in Fig. 6(a), however, $p_{1A,\max}$ is larger.

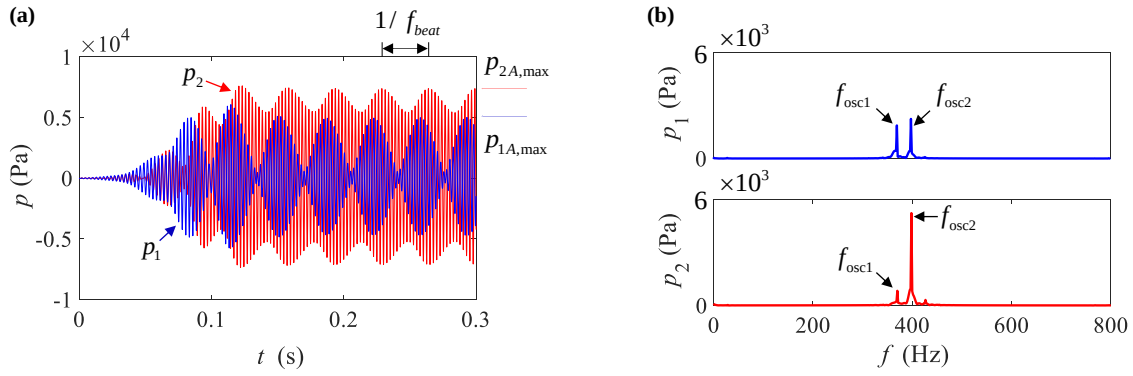

Figure 6. Dynamic behaviours of p_1 and p_2 at point B in Fig. 5. (a) Time histories. (b) FFT analyses.

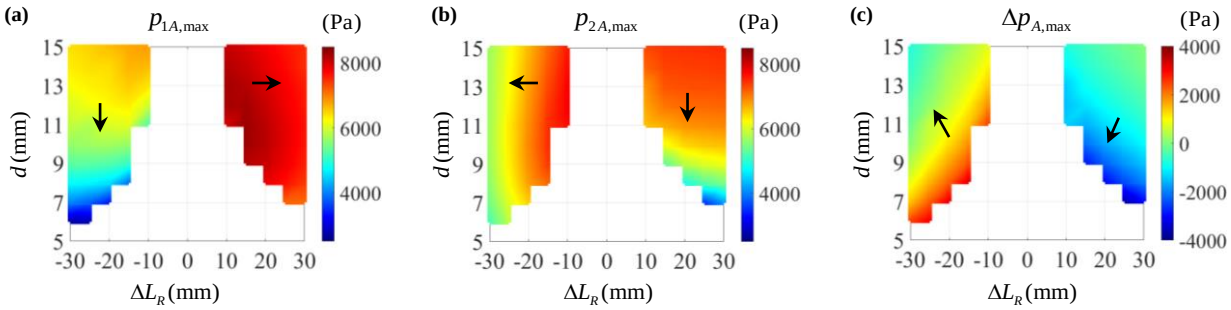

Figure 7. Contours of $p_{1A,\max}$, $p_{2A,\max}$ and $\Delta p_{A,\max} = p_{2A,\max} - p_{1A,\max}$ in region I. The arrows point to the descending direction.

It is also of interest to investigate how p_1 and p_2 in region I change as $|\Delta L_R|$ becomes smaller (or moves towards region II). Figure 8 displays the dynamic behaviours of p_1 and p_2 at point A in Fig. 5. In Fig. 8(a), $p_{1A,\max}$ and $p_{2A,\max}$ are close, and $\Delta p_{A,\max}$ approaches zero. The time difference $1/f_{beat}$ in Fig. 8(a) is smaller than that in Fig. 6(a) since a larger $|\Delta L_R|$ leads to a larger f_{beat}. In Fig. 8(b), components of f_{osc1} and f_{osc2} are observed in both p_1 and p_2. By comparing Fig. 8(b) with Fig. 6(b), it is found that, from point A to point B, the energy level of f_{osc2} increases but the energy level f_{osc1} decreases. In particular, f_{osc2} is subordinate at point A but becomes dominant in p_1 at point B. This can be viewed as the precursor of oscillator 1 being locked to f_{osc2} in region II when $\Delta L_R < 0$ (see Fig. 11). Similar conclusions can be obtained by comparing p_1 and p_2 (not shown) at point D and point E. It is found that, from point E to point D, the energy level of f_{osc1} increases but the energy level f_{osc2} decreases. f_{osc1} is always dominant in p_1, whereas the dominant component of p_2 changes from f_{osc2} at point D to f_{osc1} at point E, which is a precursor of oscillator 2 being locked to f_{osc1} in region II when $\Delta L_R > 0$ (see Fig. 11).

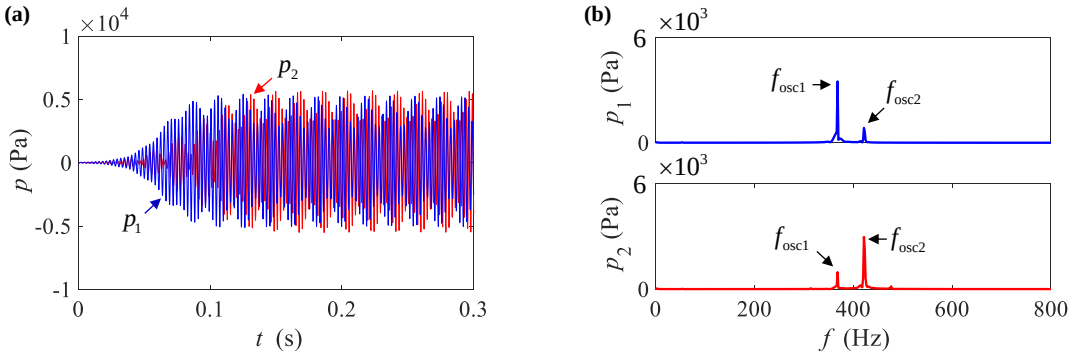

Figure 8. Dynamic behaviours of p_1 and p_2 at point A in Fig. 5. (a) Time histories. (b) FFT analyses.

4.2.3 Synchronous states

The dynamic characteristics of the synchronous states in region II are discussed in detail in this section.

Take the synchronous state at point C in Fig. 5 as an example. Figure 9 shows that in this condition, the two TA oscillators are locked to each other in both frequency and phase. In Fig. 9(a), as t increases, p_1 and p_2 develop from beating into constant-amplitude periodic oscillations whose amplitudes are denoted

by p_{1A} and p_{2A}, respectively. The dependence of oscillation frequencies f_{osc1} and f_{osc2} calculated by the reciprocal of peak-to-peak time difference on the number of acoustic cycles (denoted as N) is displayed in Fig. 9(b). It is found that f_{osc1} and f_{osc2} fluctuate along with the beats before locking at the same constant value f_{lock} at steady state. Note that f_{lock} is 390.6 Hz in the figure which is slightly larger than the natural frequencies (389.1 Hz and 375.9 Hz) of oscillator 2 and oscillator 1. The increasing trend of f_{osc1} and f_{osc2} from the beginning to the locked state coincides with the situation of reactively coupled Van der Pol oscillators. We further calculate the phase difference $\Delta\phi$ by dividing the time difference of pressure peaks between p_1 and p_2 by the time difference of two adjacent pressure peaks of p_1, as shown in Fig. 9(c). At t = 0, p_1 and p_2 are in phase. However, as the beating effect occurs, $\Delta\phi$ fluctuates around zero initially, decreases to -220° afterwards, and finally locks at a constant value $\Delta\phi_{lock}$ (= -214° or identically 146°) at steady state.

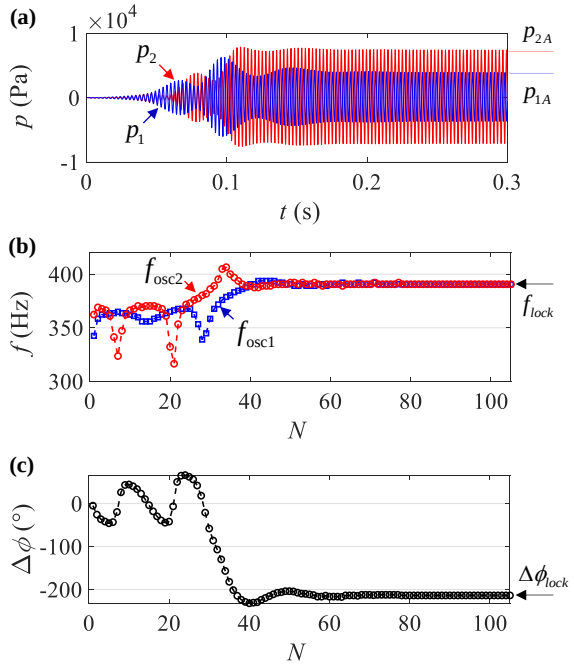

Figure 9. Dynamic behaviours of p_1 and p_2 at point C in Fig. 5. (a) Time histories. (b) Oscillation frequencies. (c) Phase difference $\Delta\phi$.

The contours of p_{1A}, p_{2A} and their difference $\Delta p_A = p_{2A} - p_{1A}$ at locked state in region II are displayed in Fig. 10. In the figure, the arrows point to the descending direction. In Figs. 10(a) and 10(b), it is found that the values of p_{1A} and p_{2A} at the outer edges of regions I are close to $p_{1A,max}$ and $p_{2A,max}$ of regions II in Fig. 7. Within region II, both p_{1A} and p_{2A} decrease as $|\Delta L_R|$ increases. Interestingly, it is found that when ΔL_R is small, p_A of locked oscillators is much larger than that of a single uncoupled oscillator. For example, at d = 5 mm and ΔL_R = 0 mm, $p_{1A} = p_{2A}$ = 8,928 Pa while p_A = 5,104 Pa of a single oscillator. The increase of p_A is primarily attributed to the fact that the radiation load between the open ends is driven by oscillators 1 and 2 in a "push and pull" manner [42]. This phenomenon implies that, under certain circumstances, mode locking is favourable for improving intensity of thermoacoustic

oscillations. In Fig. 10(c), within region II, Δp_A decreases linearly as ΔL_R increases. Specifically, $\Delta p_A > 0$ when $\Delta L_R < 0$, and $\Delta p_A < 0$ when $\Delta L_R > 0$. This feature agrees with the numerical results of single oscillators in Fig. 3: a smaller L_R has a larger p_A.

We also find that the value of Δp_A has great impact on f_{lock} and $\Delta\phi_{lock}$. As shown in Fig. 11(a), when $\Delta L_R < 0$, $p_{2A} > p_{1A}$. In this case, oscillator 2 acts as the leading external force for oscillator 1. Hence, $f_{lock} \approx f_{osc2}$. The smaller ΔL_R is, the higher f_{lock} will be. Likewise, when $\Delta L_R > 0$, $p_{2A} < p_{1A}$. In this case, oscillator 1 is the leading external force, and $f_{lock} \approx f_{osc1}$. Since f_{osc1} changes little (because L_{R1} is invariant), f_{lock} remains the same as ΔL_R increases above zero. Figure 11(b) shows the contour of $\Delta\phi_{lock}$ in region II. $\Delta\phi_{lock} < 180°$ when $\Delta L_R < 0$, $\Delta\phi_{lock} \approx 180°$ when $\Delta L_R = 0$, and $\Delta\phi_{lock} > 180°$ when $\Delta L_R > 0$. This indicates anti-phase synchronization of the two coupled TA oscillators. Such anti-phase synchronization phenomenon was also observed by Spoor and Swift [27] who utilized a narrow duct to couple two TAEs nearly the same in natural frequency.

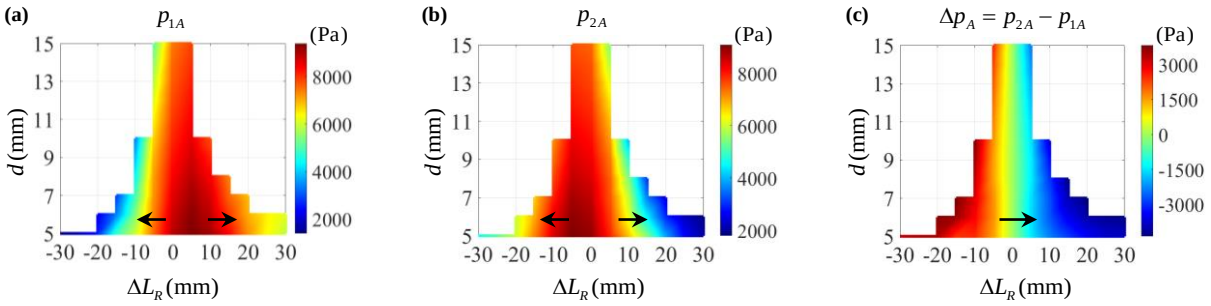

Figure 10. Contours of p_{1A}, p_{2A} and their difference Δp_A at steady state. The arrows point to the descending direction.

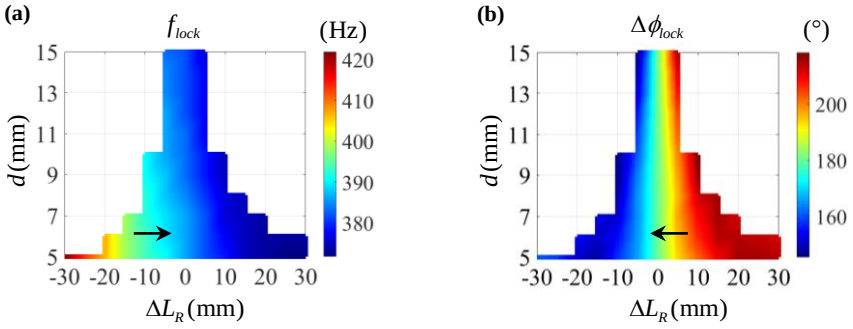

Figure 11. Contours of f_{lock} and $\Delta\phi_{lock}$ in region II. The arrows point to the descending direction.

5. Conclusions

This paper numerically investigated the mutual synchronization of two thermoacoustic (TA) oscillators that are coupled with each other via acoustic radiation at the open ends. Computational fluid dynamics (CFD) simulations were performed to reproduce the mode locking effect that was reported in previous experiments but not interpreted in a numerical way. This work also endeavoured to depict a clear picture

of the synchronization process by studying the dynamic characteristics of single, coupled asynchronous, and coupled synchronous TA oscillators. The key findings of this research are summarized as follows.

(1) The dynamic behaviour of the coupled TA oscillators is highly affected by d and ΔL_R. Two different states, asynchronous and synchronous, are identified in the two-parameter bifurcation diagram. The steady-state responses of the asynchronous and synchronous states are beating and periodic oscillations, respectively. A smaller $|\Delta L_R|$ is required to achieve the synchronous state at a larger d.
(2) Study on the asynchronous states in region I shows that both p_1 of oscillator 1 and p_2 oscillator 2 exhibit beats. The beating effect results from the superposition of acoustic waves from two TA oscillators. As $|\Delta L_R|$ moves towards region II, the energy levels of f_{osc1} and f_{osc2} in p_1 and p_2 vary. The dominant component changes from f_{osc1} to f_{osc2} in p_1 as ΔL_R (< 0) approaches region II while the dominant component changes from f_{osc2} to f_{osc1} in p_2 as ΔL_R (> 0) approaches region II.
(3) Research on the synchronous states in region II indicates that when two TA oscillators are locked to each other, the frequency and phase difference at steady state remain invariant. The locked phase difference $\Delta\phi_{lock}$ is around 180°, indicating anti-phase synchronization. The value of amplitude difference Δp_A has great impact on locked frequency f_{lock}. When $\Delta L_R < 0$, $\Delta p_A > 0$ and $p_{2A} > p_{1A}$. In this case, oscillator 2 is the leading external force, leading to $f_{lock} \approx f_{osc2}$. When $\Delta L_R > 0$, $\Delta p_A < 0$ and $p_{2A} < p_{1A}$. In this case, oscillator 1 becomes the leading external force, and $f_{lock} \approx f_{osc1}$.

This study shows that the CFD methodology offers an effective approach to study synchronization in TAEs. Prospective research will involve the simulation of other nonlinear dynamics phenomena, such as amplitude death or quenching, reported in coupled TA oscillators.

Acknowledgements

The authors want to acknowledge NESI (New Zealand eScience Infrastructure) for providing the HPC (high performance computing) service. Financial support from the Fundamental Research Funds for the Central Universities (no. 3203002101C3) is acknowledged. Fruitful discussions with Mr. Haitian Hao from Purdue University, US are highly appreciated.

References

[1] Swift GW. Thermoacoustic engines. The Journal of the Acoustical Society of America. 1988;84:1145-80.

[2] Jin T, Huang J, Feng Y, Yang R, Tang K, Radebaugh R. Thermoacoustic prime movers and refrigerators: Thermally powered engines without moving components. Energy. 2015;93:828-53.

[3] Chen G, Tang L, Mace B, Yu Z. Multi-physics coupling in thermoacoustic devices: A review. Renewable and Sustainable Energy Reviews. 2021;146:111170.

[4] Chen G, Tang L, Yu Z. Underlying physics of limit-cycle, beating and quasi-periodic oscillations in thermoacoustic devices. Journal of Physics D: Applied Physics. 2020;53:215502.

[5] Hao H, Scalo C, Sen M, Semperlotti F. Thermoacoustics of solids: A pathway to solid state engines and refrigerators. Journal of Applied Physics. 2018;123:024903.
[6] Wang K, Sun D, Zhang J, Zhang N, Luo K, Qiu L. Beating effect between a thermoacoustic source and its mechanical partner. Journal of Applied Physics. 2015;118:244907.
[7] Meir A, Offner A, Ramon GZ. Low-temperature energy conversion using a phase-change acoustic heat engine. Applied Energy. 2018;231:372-9.
[8] Tijani M, Spoelstra S. A high performance thermoacoustic engine. Journal of Applied Physics. 2011;110:093519.
[9] Xu J, Luo E, Hochgreb S. A thermoacoustic combined cooling, heating, and power (CCHP) system for waste heat and LNG cold energy recovery. Energy. 2021:120341.
[10] Rott N. Thermoacoustics. Advances in applied mechanics. 1980;20:135-75.
[11] Swift GW. Thermoacoustics: A unifying perspective for some engines and refrigerators: Springer; 2017.
[12] Swift G. Analysis and performance of a large thermoacoustic engine. The Journal of the Acoustical Society of America. 1992;92:1551-63.
[13] Gupta P, Lodato G, Scalo C. Spectral energy cascade in thermoacoustic shock waves. Journal of Fluid Mechanics. 2017;831:358-93.
[14] Biwa T, Sobata K, Otake S, Yazaki T. Observation of thermoacoustic shock waves in a resonance tube. The Journal of the Acoustical Society of America. 2014;136:965-8.
[15] Morris PJ, Boluriaan S, Shieh CM. Numerical simulation of minor losses due to a sudden contraction and expansion in high amplitude acoustic resonators. Acta Acustica united with Acustica. 2004;90:393-409.
[16] Boluriaan S, Morris PJ. Acoustic streaming: from Rayleigh to today. International Journal of aeroacoustics. 2003;2:255-92.
[17] Merkli P, Thomann H. Transition to turbulence in oscillating pipe flow. Journal of Fluid Mechanics. 1975;68:567-76.
[18] Yazaki T. Experimental observation of thermoacoustic turbulence and universal properties at the quasiperiodic transition to chaos. Physical Review E. 1993;48:1806.
[19] Yazaki T, Sugioka S, Mizutani F, Mamada H. Nonlinear dynamics of a forced thermoacoustic oscillation. Physical review letters. 1990;64:2515.
[20] Yazaki T, Takashima S, Mizutani F. Complex quasiperiodic and chaotic states observed in thermally induced oscillations of gas columns. Physical review letters. 1987;58:1108.
[21] Chen G, Tang L, Mace BR. Bistability and triggering in a thermoacoustic engine: A numerical study. International Journal of Heat and Mass Transfer. 2020;157:119951.
[22] Biwa T, Tozuka S, Yazaki T. Amplitude death in coupled thermoacoustic oscillators. Physical Review Applied. 2015;3:034006.

[23] Hyodo H, Biwa T. Stabilization of thermoacoustic oscillators by delay coupling. Physical Review E. 2018;98:052223.
[24] Penelet G, Biwa T. Synchronization of a thermoacoustic oscillator by an external sound source. American Journal of Physics. 2013;81:290-7.
[25] Sato M, Hyodo H, Biwa T, Delage R. Synchronization of thermoacoustic quasiperiodic oscillation by periodic external force. Chaos: An Interdisciplinary Journal of Nonlinear Science. 2020;30:063130.
[26] Spoor P, Swift G. The Huygens entrainment phenomenon and thermoacoustic engines. The Journal of the Acoustical Society of America. 2000;108:588-99.
[27] Spoor P, Swift G. Mode-locking of acoustic resonators and its application to vibration cancellation in acoustic heat engines. The Journal of the Acoustical Society of America. 1999;106:1353-62.
[28] Delage R, Takayama Y, Biwa T. On–off intermittency in coupled chaotic thermoacoustic oscillations. Chaos: An Interdisciplinary Journal of Nonlinear Science. 2017;27:043111.
[29] Balanov A, Janson N, Postnov D, Sosnovtseva O. Synchronization: from simple to complex: Springer Science & Business Media; 2008.
[30] Launder BE, Spalding DB. The numerical computation of turbulent flows. Numerical prediction of flow, heat transfer, turbulence and combustion: Elsevier; 1983. p. 96-116.
[31] https://wwwansyscom/products/fluids/ansys-fluent.
[32] Pope SB. Turbulent flows. IOP Publishing; 2001.
[33] Chen G, Tang L, Yu Z, Mace B. Mode transition in a standing-wave thermoacoustic engine: A numerical study. Journal of Sound and Vibration. 2021:116119.
[34] Hu L, Liu Q, Yang P, Liu Y. Identification of nonlinear characteristics of thermoacoustic oscillations in helium piping systems. International Communications in Heat and Mass Transfer. 2020:104999.
[35] Nowak I, Rulik S, Wróblewski W, Nowak G, Szwedowicz J. Analytical and numerical approach in the simple modelling of thermoacoustic engines. International Journal of Heat and Mass Transfer. 2014;77:369-76.
[36] Grossmann A, Kronland-Martinet R, Morlet J. Reading and understanding continuous wavelet transforms. Wavelets: Springer; 1990. p. 2-20.
[37] Abarbanel H. Analysis of observed chaotic data: Springer Science & Business Media; 2012.
[38] Unni VR, Prasaad YM, Ravi N, Iqbal SM, Pesala B, Sujith R. Experimental investigation of bifurcations in a thermoacoustic engine. International Journal of Spray and Combustion Dynamics. 2015;7:113-29.
[39] Sun Y, Rao Z, Zhao D, Wang B, Sun D, Sun X. Characterizing nonlinear dynamic features of self-sustained thermoacoustic oscillations in a premixed swirling combustor. Applied Energy. 2020;264:114698.
[40] Hyodo H, Biwa T. Phase-Locking and Suppression States Observed in Forced Synchronization of Thermoacoustic Oscillator. Journal of the Physical Society of Japan. 2018;87:034402.

[41] Kinsler LE, Frey AR, Coppens AB, Sanders JV. Fundamentals of acoustics, 4th Edition. pp 560 ISBN 0-471-84789-5 Wiley-VCH, December 1999. 1999:560.
[42] Hamood A, Jaworski AJ, Mao X, Simpson K. Design and construction of a two-stage thermoacoustic electricity generator with push-pull linear alternator. Energy. 2018;144:61-72.